

Brochosome-inspired binary metastructures for pixel-by-pixel thermal signature control

Zhuo Li¹, Lin Wang^{2,3}, Xiu Liu¹, Jiayu Li¹, Hyeong Seok Yun¹, Zexiao Wang¹, Xu Zhang⁴, Tak-Sing Wong^{2,3,5}, Sheng Shen^{1*}

¹Department of Mechanical Engineering, Carnegie Mellon University; Pittsburgh, PA, 15213, USA

²Department of Mechanical Engineering, The Pennsylvania State University; University Park, PA, 16802, USA

³Materials Research Institute, The Pennsylvania State University; University Park, PA, 16802, USA.

⁴Department of Electrical and Computer Engineering, Carnegie Mellon University; Pittsburgh, PA, 15213, USA

⁵Department of Biomedical Engineering, The Pennsylvania State University; University Park, PA, 16802, USA

*Corresponding author. Email: sshen1@cmu.edu

Abstract:

In nature, nano/micro-structured materials are adopted by various species to generate colors or achieve camouflage. Here, inspired by leafhopper-generated brochosomes, we design binary metastructures composed of pixel twins to achieve pixelated thermal signature control at the microscale. In the infrared range, the pixel twins exhibit distinct emissivities, creating thermal counterparts of “0-1” binary states for storing and displaying information. In the visible range, the engineered surface morphology of the pixel twins enables similar scattering behaviors, rendering the pixel twins visually indistinguishable, which achieves the camouflage of stored information. Compared to the previous work based on plasmonic holographic metasurfaces, the brochosome-like pixel twins are thermally driven, and their structure-enabled functions do not rely on permittivities of any specific material. The unique combination of visible camouflage and infrared display provides a systemic solution to the spatial control of thermal signatures, and has important implications for optical security, anticounterfeiting, and data encryption.

Teaser:

Brochosome-inspired metastructures achieve pixelated emissivity control, forming covert QR codes for infrared scanning.

Infrared radiation from objects determines their thermal signatures. Due to the incoherent, isotropic, and broadband characteristics of thermal radiation from bulk materials, precisely engineering thermal signatures, including directional (1, 2) and spectral (3, 4) control by metastructures, is critical for a wide range of energy management and conversion technologies, such as thermophotovoltaics (5–7), radiative cooling (8–11), and smart windows (12).

Meanwhile, the wide bandwidth and imperceptibility to human ocular system of thermal infrared light have enabled applications in optical security, camouflage, and encryption. With carefully designed boundary conditions (13), the isothermal contours of heated metal plates, and thus the location-dependent thermal radiation, can be manipulated to encrypt letters or patterns for viewing under infrared cameras only, which are covert in the visible range. However, thermal crosstalk between the hot and cold regions due to the diffuse heat conduction hampers the miniaturization of temperature-based spatial control of thermal signatures. To overcome this drawback, by leveraging the scattering fields from nanostructures (14–16), metasurfaces have been designed to tailor infrared wavefronts to reveal the concealed patterns and images when illuminated by lasers. Nevertheless, the requirement of external laser sources limits their applications. While advancements have been made in spatial modulation of emissivity, via phase-change materials (17, 18), nanostructured plasmonic materials (19, 20), and gated graphene (21), a universal and systematic solution for heat-driven, microscale thermal signature control is still lacking.

Here we introduce an infrared signature management solution by pixelating surfaces with a spatial resolution down to the micrometer level with a pair of micro-sized pixel twins inspired by leafhopper-produced brochosomes (Fig. 1A and inset), which are hollow spherical structures

with distributed open pores (22–24). Based on the brochosome-inspired pixel twins, we demonstrate a dual effect of concealing binary information/images in the visible range but displaying them in the infrared range via thermal excitation, without relying on external light sources such as lasers. To mimic the binary states in digital electronics, these brochosome-like pixel (BLP) twins are engineered with either open pores (op-BLPs, Fig. 1B top) or closed pores (cp-BLPs, Fig. 1B bottom), and perform as the building blocks for spatial emissivity manipulation. As illustrated in Fig. 1C, BLP twins show distinct emissivities when thermally excited, which form infrared counterparts of the binary states 0 and 1. Therefore, images can be encoded using a ‘bitmap’ consisting of the pixel twins, which can then be visualized using infrared imaging systems. This pixel-by-pixel approach employs the unique brochosome geometries, instead of specific material property for emissivity control, and thus is compatible with different substrates. Remarkably, the two types of BLPs share similar appearances when observed under visible imaging systems so that the stored patterns formed by one type of BLPs blend in with the background formed by the other, which resembles the background matching, a common camouflage strategy in nature (25, 26). To the best of our knowledge, this is the first time that a pair of microscopic structures are designed to be distinguishable in the infrared range while remaining indistinguishable in the shorter visible range, although the shorter wavelength provides a finer spatial resolution, according to the Rayleigh criterion.

Results

Brochosome-like pixels enabled visible camouflage and infrared display

The total irradiance (L) from a BLP reaching the image plane of an imaging system determines its appearance (27–29), and therefore engineering L in different wavelength ranges is crucial for the design of BLPs. The total irradiance can be expressed as:

$$L(\mathbf{x}, \mathbf{k}) = \iint f_s(\mathbf{x}, \mathbf{k}_i, \mathbf{k}) L_i(\mathbf{x}, \mathbf{k}_i) \cos \theta_i d\mathbf{x} + L_e(\mathbf{x}, \mathbf{k}), \quad (1)$$

where $L(\mathbf{x}, \mathbf{k})$ represents the total irradiance from the location \mathbf{x} on the surface of a BLP with a wave vector \mathbf{k} (see Fig. 2A for notations). In Eq. 1, the first term on the right-hand side represents the scattering of the BLP (blue arrow in Fig. 2A) with respect to the light source $L_i(\mathbf{x}, \mathbf{k}_i)$, and the surface integration encompasses the illuminated surface of the BLP.

$f_s(\mathbf{x}, \mathbf{k}_i, \mathbf{k})$ is the bi-directional scattering distribution function (BSDF) that characterizes the scattering behavior. The second term, $L_e(\mathbf{x}, \mathbf{k})$, accounts for thermal emission from the BLP (red arrow in Fig. 2A), which mainly occupies the infrared spectrum when the BLP is thermally excited to a temperature slightly above room temperature, based on Wien's displacement law. Clearly, in the visible range, Eq.1 is dominated by the scattering term due to the negligible contribution from emission, while the emission term $L_e(\mathbf{x}, \mathbf{k})$ reveals the key electromagnetic behaviors of BLPs in the infrared range. To facilitate the short-wavelength camouflage and long-wavelength display, it is desired that the two types of BLPs exhibit similar visible scattering while having distinct infrared emission. We performed finite difference time domain (FDTD) simulations for op-BLPs and cp-BLPs in both the infrared and visible ranges (see Methods). The diameters of pores (d) and BLPs (D) (see Fig. S1, B and D) are the key design parameters. We started the design process by adopting the ratio $d/D = 0.28$, which is an average derived from

natural brochosomes (30) produced by diverse leafhoppers, as shown in Fig. 2B. Subsequently, the ratio was optimized to achieve the desired camouflage and display functions, and then the size of BLPs can be chosen according to the target working wavelengths. Here, the diameter D and pore size d of BLPs are set to be 20 μm and 3.7 μm , respectively, for our infrared measurements (see Methods). The material of BLPs is chosen to be nickel (Ni) or other reflective metals, which provide a high permittivity contrast between the BLPs and the environment.

In the visible range, we simulated the BSDFs of both types of BLPs to demonstrate their scattering behaviors. Conventionally, determining $\text{BSDF}(\theta_o, \theta_i)$ requires the simulations/measurements of the energy distribution at any given scattering angle θ_o with respect to illuminations from various directions θ_i , as marked in Fig. 2A. Given that optical microscopies utilized for observing microscale BLPs usually have illuminations primarily from the vertical direction, we limited the visible range simulation of the BLPs to the scattering distribution functions with respect to the normal illumination only, i.e., $\text{BSDF}(\theta_o, \perp)$. In Fig. 2C, we compared the simulated results for both op-BLPs (solid lines) and cp-BLPs (dashed lines) at various visible wavelengths. The similarity of BSDFs between the two types of BLPs can be attributed to the identical arrangement (20, 31) of surface features (either open pores or closed pores, see Supplementary Note). Such similar BSDFs ensure that the pixel twins cannot be easily distinguished under visible imaging systems, thereby establishing an effective visible camouflage effect.

In the infrared range, we calculated the spectral absorption cross sections (σ) for both types of BLPs. The magnitude of σ also indicates the emission capability of the two structures, based on

Kirchhoff's law (29). Figure 2D showed the results for a single op-BLP and cp-BLP. For comparison, we included the results for a Ni sphere with the same diameter (20 μm). Within the wavelength range from 2.5 μm to 8 μm , the op-BLP showed an enhanced absorption cross section, compared to those of the cp-BLP and the sphere. The contrast of σ between the op-BLP and cp-BLP structures can be further illustrated in Fig. 2E, where we plotted their excess absorption cross section ($\Delta\sigma = \sigma_{\text{BLP}} - \sigma_{\text{sphere}}$) relative to that of the sphere. The enhanced σ of the op-BLP within this wavelength range can be explained by the exposed cavity formed by its open pores. As shown in Fig. 2, F and G, the electromagnetic field penetrates the op-BLP (Fig. 2F), becomes trapped within the exposed cavity, and eventually gets absorbed due to the electron damping effect of Ni. Conversely, this cavity effect remains absent in the cp-BLP (Fig. 2G), which results in the contrast of σ between these two structures. It is worth noting that such a high contrast gradually decreases after it reaches the maximum at the wavelength around 5 μm , because the long-wavelength electromagnetic waves cannot penetrate BLPs even with the existence of the open pores (Fig. S2). Here, we designed the size of BLPs to ensure a strong infrared contrast over the entire working range of our infrared imaging system (see Methods), but it can be optimized for other wavelengths as well. Also, the unique multi-pore configuration of BLPs is crucial to achieve the high contrast because simple spherical structures with fewer or only one open pore will reduce the amount of light reaching the cavity, thus leading to diminished absorption cross sections (Fig. S3A).

Thermal-optical characterization of brochosome-like pixels

To quantify the emission contrast, we fabricated BLP arrays of both kinds and measured their spatial distributions of emissivity using an infrared thermal mapping system (see Methods). In Fig. 3, A and B, both the 9-by-9 BLP arrays were fabricated by the two-photon polymerization

and subsequently coated with ~100 nm Ni (see Fig. S4 for the enlarged scanning electron microscope (SEM) images and the X-ray element mapping results). Figure 3, C and D, plot the spatial distributions of the measured emissivity for the op-BLP and cp-BLP arrays, respectively, from which the spatially averaged emissivities were calculated based on the central 7 by 7 BLPs (the BLPs located at the edges are excluded due to the edge effect). The measured average emissivities are 0.4189 and 0.3073 for the op-BLP and cp-BLP arrays, respectively, and they agree well with our simulation results, 0.449 and 0.301, which are acquired by integrating simulated spectral-directional emissivity $\varepsilon_{\lambda,\theta}$ (Fig. 3, E and F) for both arrays, respectively (see Methods). The spectral contrast in infrared emissivity for both arrays can be further revealed by the Fourier transform infrared (FTIR) measurements (see Fig. S3B).

Notably, the interstices between neighboring BLPs in both arrays showed high emissivities (~0.5) because they also act as optical cavities and thus enhance the local emission, which compromises the emissivity contrast between BLP arrays of different kinds. By calculating the average local emissivities within arbitrarily selected regions containing only individual BLPs (insets of Fig. 3, C and D), the emissivities of single op-BLPs and cp-BLPs were estimated to be 0.3329 and 0.1329, respectively, which gives rise to an emissivity contrast ratio of approximately 2.5: 1. In comparison, the optical images (shown in Fig. S5, A and B) of the two arrays were analyzed via the quantitative color pattern analysis method (32), which showed well matched pattern energy distributions (Fig. S5C), indicating the visual indistinguishability of the two arrays to human eyes at visible wavelengths.

Experimental demonstration of visible camouflage and infrared display

The BLP twins represent a pair of binary states under infrared imaging systems due to their emissivity contrast, whereas their nearly identical visible scattering behaviors render them almost indistinguishable to human eyes. Such a wavelength-dependent distinguishability lays the foundation for their camouflage and display functionalities in the visible and infrared ranges, respectively. We optimized the design of BLPs by studying the influence of the pore shape and size on the proposed camouflage and display functions. Considering the naturally occurring hexagonal and pentagonal open pores found in leafhopper-produced brochosomes (inset of Fig. 1A), we designed the BLP arrays composed of op-BLPs and cp-BLPs with polygonal pores in addition to the round ones, as shown in Fig. 4A-i for the shape map and Fig. 4A-ii for the SEM images. The array was then examined under both an optical microscope (Fig. 4A-iii) and an infrared microscope (Fig. 4A-iv) at the same magnification. Our observations indicate that variation in pore shape has minimal impact on their performance. Based on the round-pore design, we fabricated another array incorporating BLPs with varying pore sizes (Fig. 4B), from which we found while increasing the diameter of pores enhances the infrared emissivity contrast between the two pixels, it concurrently diminishes the visual concealment between the two structures.

Utilizing the optimized BLPs ($D = 20 \mu\text{m}$ and $d = 3.7 \mu\text{m}$, round pores), we demonstrated the pixel-by-pixel camouflage and display functions by combining the BLP arrays. Figure 4C-i shows a SEM image of two BLP arrays, where we patterned the letters ‘C’ and ‘P’ using the cp-BLPs within the background formed by op-BLPs. The square-packed $20 \mu\text{m}$ -diameter BLP pixels result in an effective pixel density of 1270 pixel per inch, which is more than 5 times

denser than typical micro-LED displays used in smart devices (33), and the BLPs can also be closely packed into a hexagonal lattice for an even greater pixel density (see Fig. S6). Figure 4C-ii demonstrates the visible camouflage effect observed through an optical microscope with a 20× magnification objective, from which the two kinds of BLPs are indistinguishable so that the patterns are buried into the background. However, the emissivity difference between the two types of BLPs offers a pronounced contrast to display the hidden patterns in the infrared range, as shown in Fig. 4C-iii, which is captured at the same magnification but with an infrared microscope. Figure 4C-iv plots the calculated spatial distribution of emissivity from Fig. 4C-iii, where the typical emissivities of each individual op-BLPs and cp-BLPs are approximately 0.35 and 0.15, further verifying the theoretical contrast ratio of around 2.5: 1. Furthermore, due to the highly symmetrical arrangement of pores on the BLP surfaces, the infrared emission contrast between the two kinds of pixels can be maintained even when viewed from different angles. As shown in Fig. S7, the ‘C’ and ‘P’ patterns remain discernable under infrared microscopes when tilted by a small angle ($\sim 6^\circ$ achieved by our experimental setup), thus accommodating angular misalignments during the view process. It is worth noting that the maximum viewing angle is not limited by the BLPs but rather the focal depth of the infrared microscope. We further quantify the camouflage and display capabilities of the BLPs by counting the pixel fractions at different brightness level (see Fig. S8) based on the method in Ref (34). This analysis revealed that the BLPs preserve the camouflage ability even under dark field imaging in the visible range.

We extended the application of BLPs by crafting a BLP array patterned into a QR code (version 1, ECC level L) containing the web address of Carnegie Mellon University, where the cp-BLPs formed the QR code while the op-BLPs composed the background, as shown in Fig. 4D. The

dimension of the QR code is 21 pixel by 21 pixel with a 2-pixel margin on each sides, resulting in a physical size of 0.5 mm by 0.5 mm. Compared with other nano/microstructure-based QR codes, our pixel size as well as overall QR code dimensions are much smaller than those based photonic crystals (35, 36), and on par with those derived from imprinted polyvinyl alcohol nanostructures (37), especially given that our QR code is designed to work at a significantly longer wavelength. The QR code remains effectively camouflaged when subjected to the visible range scanning, as shown in Fig. 4D-ii for the visible optical image. Conversely, the infrared images of the BLP pixel array (Fig. 4D-iii) and calculated emissivity (Fig. 4D-iv) clearly display the encrypted QR code, thus allowing rapid scanning using common QR code scanning applications on smart devices (see Movie S1). In practice, slightly blurring the infrared images of the BLP QR code by defocusing the infrared microscope or applying Gaussian filters (38, 39) can mitigate the local emissivity variations within single BLPs to better manifest the binary digits akin to traditional QR codes, which will make the BLP QR code easier to scan (see Fig. S9).

Discussion

To summarize, inspired by leafhopper-generated brochosomes, we created a pair of BLP twins with either open pores or closed pores. Based on the unique emissive and scattering properties of the BLP twins, we developed a pixel-by-pixel approach for spatial thermal signature control and demonstrated a dual effect of visible camouflage and infrared display via thermal excitation. The BLP-based camouflage effect under visible range imaging systems arises from their similar visible scattering behaviors, while the high emissivity contrast (2.5:1) between the two types of BLPs enables the thermal display of the concealed information by infrared imaging systems. Although it is well known that the shorter wavelength provides a finer spatial resolution based on

the Rayleigh criterion, for the first time, we designed a metastructure pair to be distinguishable in the infrared range but indistinguishable in the visible range. Using the BLP twins as the fundamental building blocks, our BLP design and pixel-by-pixel approach allow for systemic and scalable control of thermal signatures, which paves the way for various optical security applications, such as anticounterfeiting and encryption.

List of figures

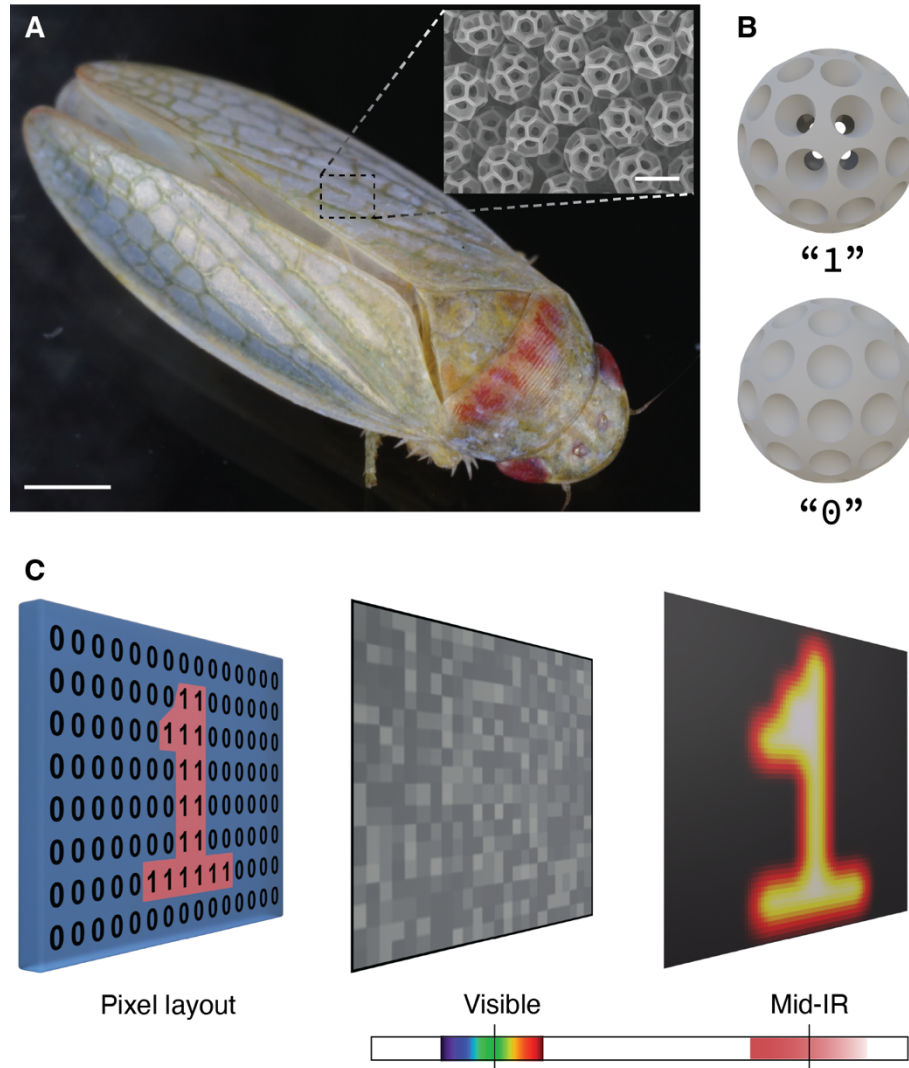


Fig. 1 | Thermal signature manipulation by brochosome-like pixels. (A) An optical image of a leafhopper *Gyponana Serpenta*. Scale bar: 1 mm. Insets: a scanning electron microscopy (SEM) image of leafhopper generated brochosomes. Scale bar: 500 nm. (B) Top to bottom, 3D models of brochosome-like pixels (BLPs) with open pores (op-BLPs) and closed pores (cp-BLPs), respectively. (C) Schematic of information camouflage and BLPs. Information is concealed in the binary array formed by BLPs, which is camouflaged in the visible range but can be displayed under infrared imaging systems.

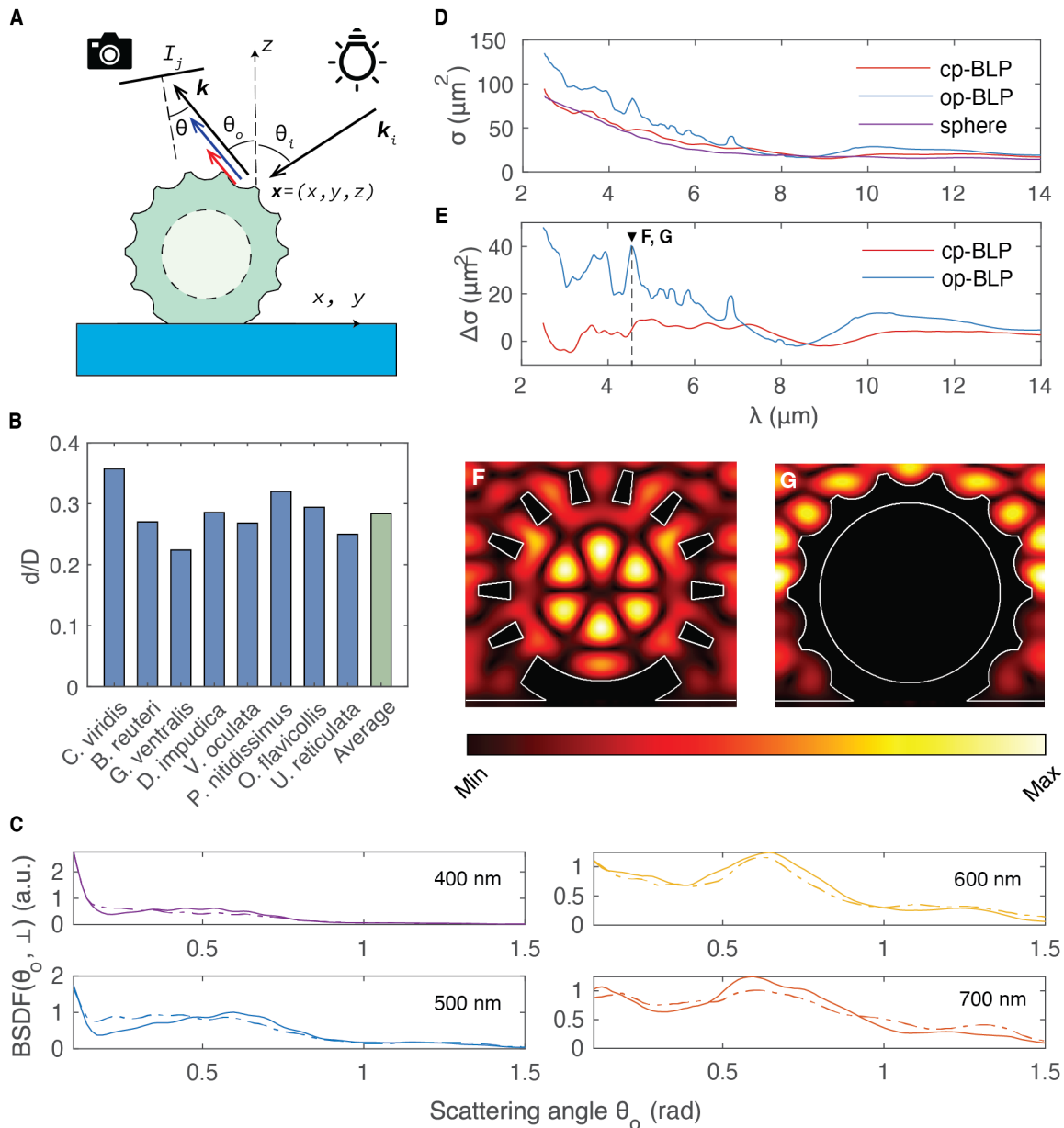


Fig. 2 | Multispectral design of brochosome-like pixels (BLPs). (A) Schematic of light-BLP interactions. (B) Pore diameter to BLP diameter ratio d/D of natural brochosomes produced by various leafhoppers, from which an averaged ratio of 0.28 is acquired and used as the initial design of the BLPs. Data are acquired from Ref. (30). (C) Simulated bi-directional scattering distribution functions in the visible range for both a cp-BLP (solid lines) and an op-BLP (dash-dot lines) with respect to normal illumination. (D) Simulated absorption cross-sectional areas σ of a BLP with open pores (op-BLP), a BLP with closed-pores (cp-BLP), and a sphere. The outer diameter of the simulated BLPs and sphere is $20\ \mu\text{m}$, and the material is nickel (Ni). (E) Excess absorption cross-sectional areas $\Delta\sigma$ of BLPs compared to the sphere. (F) – (G) Simulated spatial distribution of the magnitude of the electrical field ($\lambda = 4.5\ \mu\text{m}$, marked by the dashed line in panel E) near an op-BLP and a cp-BLP, respectively.

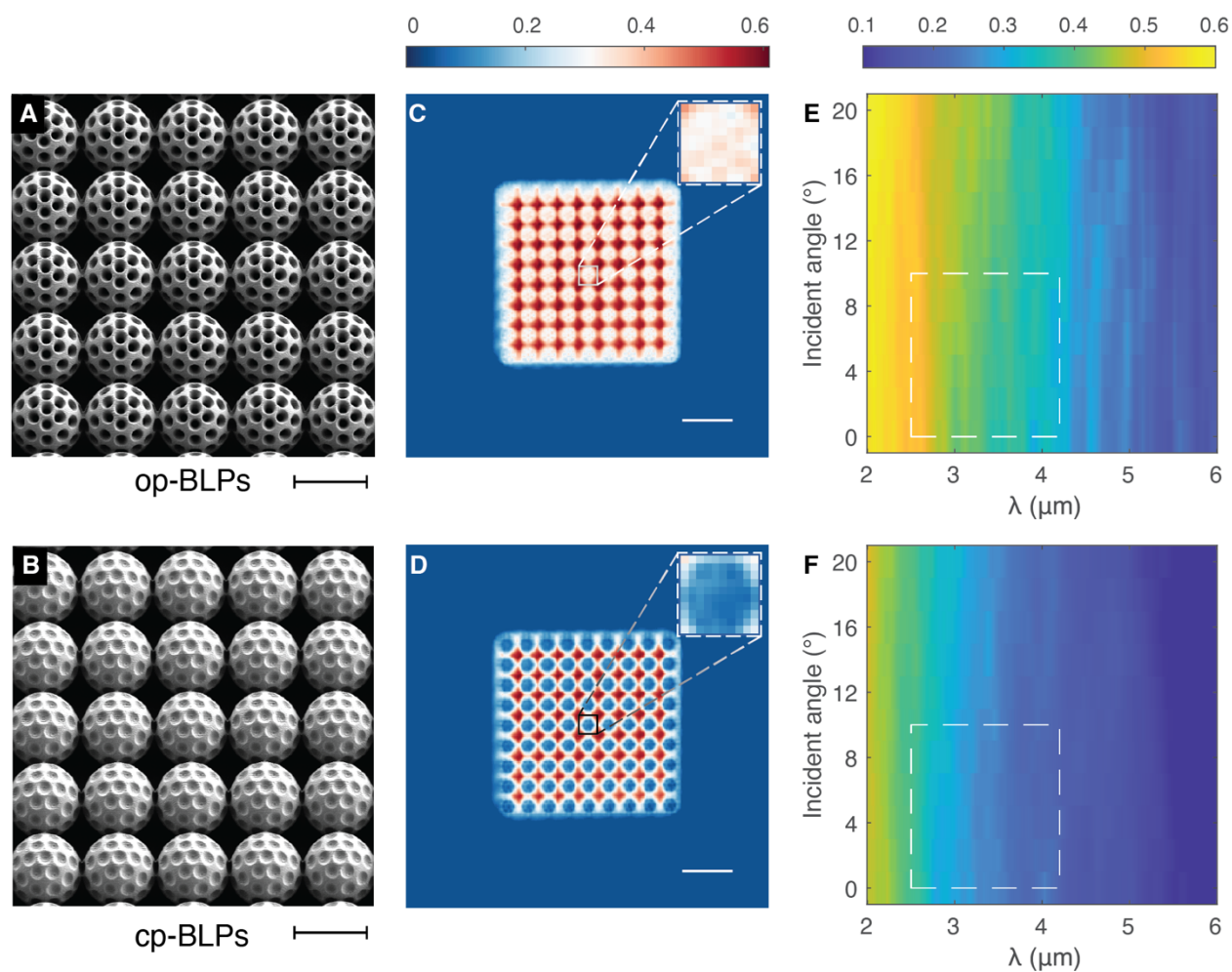


Fig. 3 | Emissivity contrast of brochosome-like pixels. (A) – (B) SEM images of fabricated op-BLP array and cp-BLP arrays, respectively. Scale bar: 20 μm . (C) – (D) Measured spatial distribution of emissivities of op-BLP and cp-BLP arrays, respectively. Scale bar: 50 μm . Insets: Typical local enlarged images of single BLPs from which their emissivities are evaluated. (E) – (F), Simulated spectral-directional absorptivity of op-BLP and cp-BLP arrays, respectively. The averaged emissivities can be calculated according to Eqs. M1 to M3, in which the integration domains are marked by the white boxes.

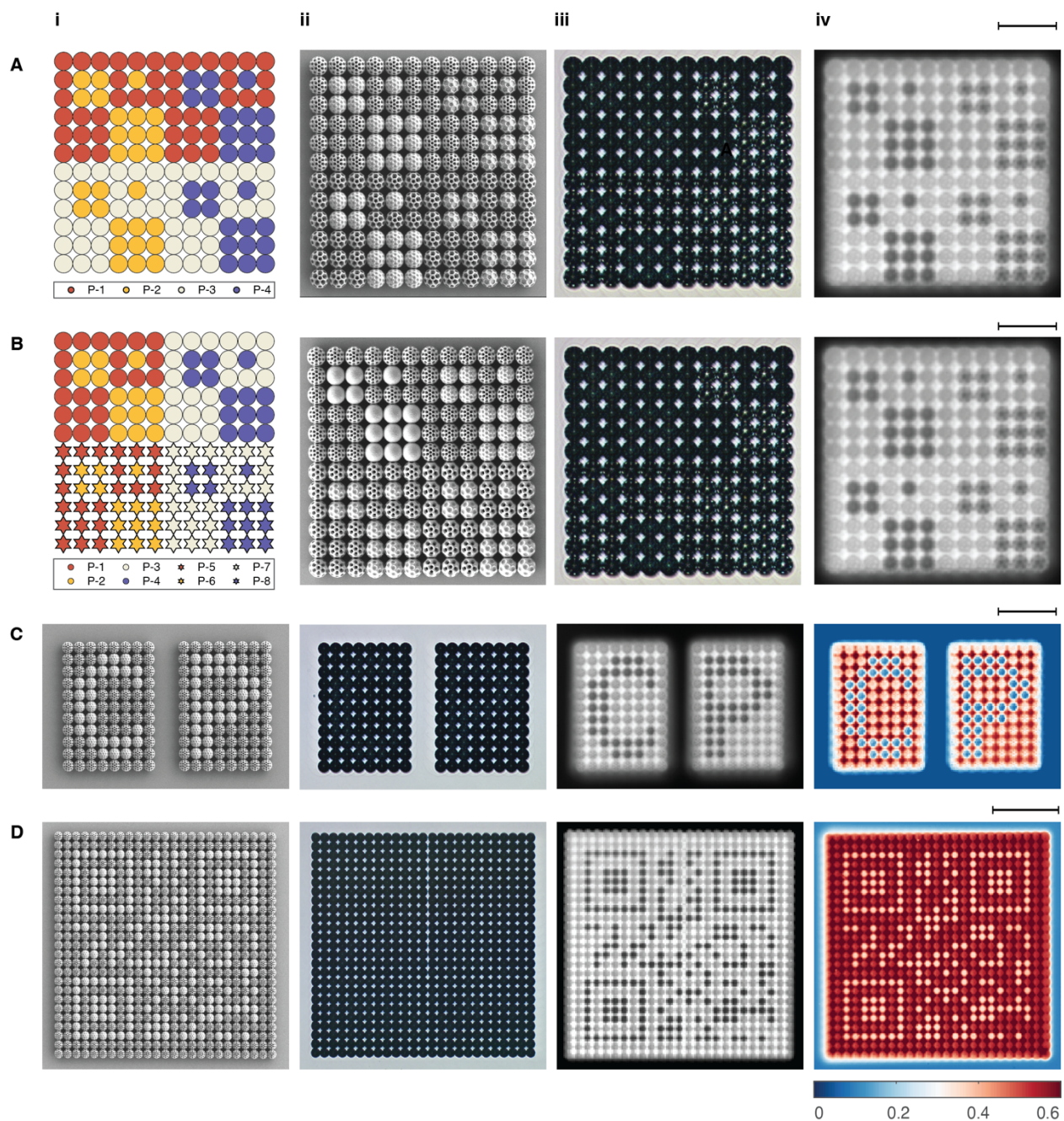


Fig. 4 | Visible camouflage and infrared display based on optimized brochosome-like pixels. (A) – (B) Optimization of the shape and size of pores in BLPs, respectively. Scale bar: 60 μm . In B-I, Design of the BLPs array, with P-1 to P-4 represent BLPs with round open pores, round closed pores, polygon open pores, and polygon closed pores, respectively. The diameter of round pores is 3.7 μm , and diameter of polygon pores is 4.5 μm . In B-i, P-1 to P-8 represent op-BLPs with $d = 3.7 \mu\text{m}$, bare spheres, op-BLPs with $d = 4.0 \mu\text{m}$, cp-BLPs with $d = 4.0 \mu\text{m}$, op-BLPs with $d = 5.0 \mu\text{m}$, cp-BLPs with $d = 5.0 \mu\text{m}$, op-BLPs with $d = 6.0 \mu\text{m}$, and cp-BLPs with $d = 6.0 \mu\text{m}$, respectively. In (A) – (B), ii to iv, a scan electron microscopy (SEM) image, an optical

image, and an infrared image of the designed BLP arrays. For the best visible camouflage and infrared display effect, combination of round op/cp-BLPs were used in the demonstration (red and yellow combination in panel A-i). **(C)** BLP array forming letters ‘C’ and ‘P’. Scale bar: 100 μm . **(D)** BLP array forming a QR code (storing the address of the homepage of Carnegie Mellon University). Scale bar: 150 μm . In **(C) – (D)**, i, SEM images of the BLP array; ii, optical images of the BLP arrays. The patterns are camouflaged through background matching; iii – iv, infrared images and calculated spatial distribution of emissivity based on the infrared images, displaying patterns due to the emissivity contrast between different BLPs.

Methods

Design and modeling of brochosome-like pixels

The design and 3D modeling of brochosome-like particles (BLPs) are conducted in SolidWorks, a computer-aided design software. The designed structures are then exported as standard triangle language files (.stl) for optical simulations and fabrications. The 3D and cross-sectional views of both a BLP with open pores (op-BLP) and with closed pores (cp-BLP) are shown in Fig. S1, A to D, respectively. Each BLP has 6 loops of pores evenly distributed among the surface. Each loop contains from top to bottom, 1, 6, 10, 14, 14, and 10 pores, respectively. The diameter of pores d and the diameter of BLPs D (shown in Fig. S1, B and D) are the key design parameters. We started the design by adopting the ratio $d/D = 0.28$, which is the average value acquired from natural brochosomes generated by various of leafhoppers (Fig. 2B), and then optimized such ratio for best wavelength-dependent distinguishability between the two BLPs (Fig. 4, A and B). The actual size of the BLPs is designed to ensure strong infrared contrast between the two structures within the entire working wavelength range of the infrared imaging systems (2.5 to 4.2 μm). Results shown in the main text are achieved with BLPs with $D = 20 \mu\text{m}$ and $d = 3.7 \mu\text{m}$.

FDTD simulation of brochosome-like pixels

The finite-difference time-domain (FDTD) simulations of the BLPs were conducted in Ansys Lumerical FDTD Solutions with the .stl files generated by SolidWorks. The diameter of single BLPs is scaled to 20 μm . The material of the BLPs is set to Nickel (Ni); a silicon (Si) substrate (the blue block in Fig. 1a), coated with 100 nm thick Ni, is also considered in simulations. Both the materials are characterized by their permittivities, which are acquired from (40).

In the simulations of absorption cross section σ of single BLPs, the total-field scattered-field source is used to excite the BLPs and σ is calculated by a built-in analysis module, absorption analysis group, of the software. To generate the field profiles, single BLPs are excited by a plane wave source linearly polarized along the x direction and propagating along the z direction, and a frequency-domain field profile monitor is used to capture the field profiles at the central cross section of the BLPs parallel to the z-axis (see Fig. 1A for the coordinate system). Perfectly matched layers (PMLs) are used in both simulations as boundary conditions to remove unphysical echoes. For the simulations of scattering distribution function of the BLPs, a plane wave source (polarized along the x direction and propagates along the z direction) with Gaussian profiles is used to illuminate single BLPs, and a 80 μm by 80 μm 2D power monitor parallel to the x-y plane located 13.5 μm away from the center of the BLPs is used to capture the Poynting vectors of the scattered field, which are then projected to the far field through the built-in module, far-field projection, of the software to calculate the angular distribution. In the simulations regarding the spectral-directional absorptivity (SDA) of BLP arrays, the plane wave source with the type of ‘broadband fixed angle source technique’ is used to illuminate one unit cell. The boundary conditions at directions transverse to the source propagation direction are handled by the software, and the rest boundary conditions are set to PMLs. To be comparable with up-polarized thermal absorption/emission, simulated SDAs shown in the Fig. 3 are averaged over both the S and P polarization states. Then the averaged SDAs are integrated to calculate the overall emissivity (29):

$$\varepsilon = \frac{1}{AB} \int_{\lambda_{\min}}^{\lambda_{\max}} d\lambda \int_0^{\theta_{\max}} \varepsilon_{\lambda,\theta} \sin\theta \cos\theta E_{\lambda,b}(\lambda, T) d\theta, \quad (\text{M1})$$

where

$$A = \int_0^{\theta_{\max}} \sin\theta \cos\theta d\theta, \quad (\text{M2})$$

and

$$B = \int_{\lambda_{\min}}^{\lambda_{\max}} E_{\lambda,b}(\lambda, T) d\lambda, \quad (\text{M3})$$

in which $E_{\lambda,b}(\lambda, T)$ represents the blackbody radiation. θ_{\max} , λ_{\min} , λ_{\max} , and T are set to 10° , $2.5 \mu\text{m}$, $4.2 \mu\text{m}$, and 323.15 K , respectively, to match with the specifications of the thermal mapping system used in measurement.

Fabrication of brochosome-like pixels

The BLP arrays were fabricated by two photon polymerization 3D printing method with the 3D files of BLPs (.stl) designed in SolidWorks. The 3D printing process was executed by a 3D printer Nanoscribe, which prints structures with a resolution of 100 nm. Specifically, the photoresist IP-DIP of about 50 μL was added onto a silicon substrate and the photoresist will be polymerized by a laser beam of 780 nm. The BLP structures were printed while the focus point of the laser beam moves spatially as directed by the 3D modeling file. Finally, the uncured polymer was removed by immersing sample into the SU-8 developer for 10 mins and then the sample was rinsed with isopropyl alcohol for 2 minutes. After that the 3D printed BLPs were sputter coated conformally with a layer of 100 nm nickel using the e-beam sputter machine (Temescal FC-2000, Ferrotec, USA). The temperature of the samples during the sputtering process was maintained around 289.15 K (16 $^\circ\text{C}$).

Characterization of brochosome-like pixels

The fabricated BLP samples are characterized in multiple ways. The morphologies of the fabricated samples are examined under a scanning electron microscopy (Merlin, Zeiss, Germany) for quality control. The infrared images are taken by the thermal mapping system (QFI

InfraScope) with a 20× magnification objective (12× for the QR code sample, and the tilted measurement shown in Fig. S8). The thermal mapping system captures the infrared emission from the samples within the wavelength range from 2.5 μm to 4.2 μm and normalizes it to the blackbody emission to calculate the emissivity. During the infrared imaging process, the BLP samples are heated to 323.15 K (50 °C) by a Linkam HFS600 thermal stage. The infrared reflection spectrum of the two samples shown in Fig. 3 are measured by the Fourier-transform infrared microscope (Nicolet Continuum). Note that due to the spherical shape of BLPs, the reflected light is distributed in the upper hemispherical space, so the majority of which cannot be received by the FTIR system, resulting in the extremely low measured reflectivity. So, it cannot be used to estimate the absorptivity/emissivity of the structure.

The optical images of the BLP arrays were taken by Nikon digital sight DS-Fi1 with a 20× magnification objective (10× for the QR code sample). The similarity/indistinguishability of the images of different BLP arrays is assessed by the quantitative color and pattern analysis method (32), implemented in the Mica Toolbox. Specifically, images of both the op-BLP and cp-BLP (Fig. S5, A and B) arrays discussed in Fig. 3 were captured with the same illumination and camera settings are imported to the software, where the significance/notability (measured in pattern energy) are analyzed for features of different sizes (measured in pixel) in the images. Figure S5C compared the pattern energy distribution of the two images, which overlap with each other, indicating a high degree of similarity between them to human eyes.

References

1. J. Xu, J. Mandal, A. P. Raman, Broadband directional control of thermal emission. *Science*. 372, 393–397 (2021).
2. S. Fan, Thermal Photonics and Energy Applications. *Joule*. 1, 264–273 (2017).
3. P. N. Dyachenko, S. Molesky, A. Y. Petrov, M. Störmer, T. Krekeler, S. Lang, M. Ritter, Z. Jacob, M. Eich, Controlling thermal emission with refractory epsilon-near-zero metamaterials via topological transitions. *Nature Communications*. 7, 11809 (2016).
4. L. P. Wang, Z. M. Zhang, Wavelength-selective and diffuse emitter enhanced by magnetic polaritons for thermophotovoltaics. *Applied Physics Letters*. 100, 63902 (2012).
5. X. Dang, J. Qi, M. T. Klug, P.-Y. Chen, D. S. Yun, N. X. Fang, P. T. Hammond, A. M. Belcher, Tunable Localized Surface Plasmon-Enabled Broadband Light-Harvesting Enhancement for High-Efficiency Panchromatic Dye-Sensitized Solar Cells. *Nano Letters*. 13, 637–642 (2013).
6. S. Molesky, Z. Jacob, Ideal near-field thermophotovoltaic cells. *Physical Review B - Condensed Matter and Materials Physics*. 91 (2015), doi:10.1103/PhysRevB.91.205435.
7. B. Zhao, L. Wang, Y. Shuai, Z. M. Zhang, Thermophotovoltaic emitters based on a two-dimensional grating/thin-film nanostructure. *International Journal of Heat and Mass Transfer*. 67, 637–645 (2013).
8. E. Rephaeli, A. Raman, S. Fan, Ultrabroadband Photonic Structures To Achieve High-Performance Daytime Radiative Cooling. *Nano Letters*. 13, 1457–1461 (2013).
9. T. Li, Y. Zhai, S. He, W. Gan, Z. Wei, M. Heidarinejad, D. Dalgo, R. Mi, X. Zhao, J. Song, J. Dai, C. Chen, A. Aili, A. Vellore, A. Martini, R. Yang, J. Srebric, X. Yin, L. Hu, A radiative cooling structural material. *Science (New York, N.Y.)*. 364, 760–763 (2019).
10. A. P. Raman, M. A. Anoma, L. Zhu, E. Rephaeli, S. Fan, Passive radiative cooling below ambient air temperature under direct sunlight. *Nature* 2014 515:7528. 515, 540–544 (2014).
11. J. Yun, D. Chae, S. So, H. Lim, J. Noh, J. Park, N. Kim, C. Park, H. Lee, J. Rho, Optimally Designed Multimaterial Microparticle–Polymer Composite Paints for Passive Daytime Radiative Cooling. *ACS Photonics*. 10, 2608–2617 (2023).
12. X. H. Li, C. Liu, S. P. Feng, N. X. Fang, Broadband Light Management with Thermochromic Hydrogel Microparticles for Smart Windows. *Joule*. 3, 290–302 (2019).
13. R. Hu, S. Huang, M. Wang, X. Luo, J. Shiomi, C. W. Qiu, Encrypted Thermal Printing with Regionalization Transformation. *Advanced Materials*. 31, 1–7 (2019).
14. X. Xie, X. Li, M. Pu, X. Ma, K. Liu, Y. Guo, X. Luo, Plasmonic Metasurfaces for Simultaneous Thermal Infrared Invisibility and Holographic Illusion. *Advanced Functional Materials*. 28, 1706673 (2018).
15. G. Cao, H.-X. Xu, L.-M. Zhou, Y. Deng, Y. Zeng, S. Dong, Q. Zhang, Y. Li, H. Yang, Q. Song, X. Liu, Y. Li, C.-W. Qiu, Infrared metasurface-enabled compact polarization nanodevices. *Materials Today*. 50, 499–515 (2021).
16. J. Kim, J. Seong, W. Kim, G.-Y. Lee, S. Kim, H. Kim, S.-W. Moon, D. K. Oh, Y. Yang, J. Park, J. Jang, Y. Kim, M. Jeong, C. Park, H. Choi, G. Jeon, K. Lee, D. H. Yoon, N. Park, B. Lee, H. Lee, J. Rho, Scalable manufacturing of high-index atomic layer–polymer hybrid metasurfaces for metaphotonics in the visible. *Nature Materials*. 22, 474–481 (2023).

17. C. Kim, Y. Kim, M. Lee, Laser-Induced Tuning and Spatial Control of the Emissivity of Phase-Changing Ge₂Sb₂Te₅ Emitter for Thermal Camouflage. *Advanced Materials Technologies*. 7, 2101349 (2022).
18. Z. Xu, Q. Li, K. Du, S. Long, Y. Yang, X. Cao, H. Luo, H. Zhu, P. Ghosh, W. Shen, M. Qiu, Spatially Resolved Dynamically Reconfigurable Multilevel Control of Thermal Emission. *Laser & Photonics Reviews*. 14, 1900162 (2020).
19. Z. J. Coppens, J. G. Valentine, Spatial and Temporal Modulation of Thermal Emission. *Advanced Materials*. 29, 1701275 (2017).
20. D. Franklin, S. Modak, A. Vázquez-Guardado, A. Safaei, D. Chanda, Covert infrared image encoding through imprinted plasmonic cavities. *Light: Science & Applications*. 7, 93 (2018).
21. O. Salihoglu, H. B. Uzlu, O. Yakar, S. Aas, O. Balci, N. Kakenov, S. Balci, S. Olcum, S. Süzer, C. Kocabas, Graphene-Based Adaptive Thermal Camouflage. *Nano Letters*. 18, 4541–4548 (2018).
22. G. S. Tulloch, J. E. Shapiro, Brochosomes and Leafhoppers. *Science*. 120, 232–232 (1954).
23. R. Rakitov, S. N. Gorb, Brochosomes protect leafhoppers (Insecta, Hemiptera, Cicadellidae) from sticky exudates. *Journal of The Royal Society Interface*. 10, 20130445 (2013).
24. S. Yang, N. Sun, B. B. Stogin, J. Wang, Y. Huang, T. S. Wong, Ultra-antireflective synthetic brochosomes. *Nature Communications*. 8, 1–8 (2017).
25. M. Stevens, S. Merilaita, Animal camouflage: current issues and new perspectives. *Philosophical Transactions of the Royal Society B: Biological Sciences*. 364, 423–427 (2009).
26. S. Merilaita, J. Lind, Background-matching and disruptive coloration, and the evolution of cryptic coloration. *Proceedings of the Royal Society B: Biological Sciences*. 272, 665–670 (2005).
27. K. Vynck, R. Pacanowski, A. Agreda, A. Dufay, X. Granier, P. Lalanne, The visual appearances of disordered optical metasurfaces. *Nature Materials*. 21, 1035–1041 (2022).
28. M. Pharr, W. Jakob, G. Humphreys, *Physically Based Rendering (Morgan Kaufmann, Burlington, MA, ed. 3rd, 2017)*.
29. T. Bergman, A. Lavine, F. Incropera, D. Dewitt, *Fundamentals of heat and mass transfer (John Wiley & Sons, Inc, Hoboken, NJ, ed. 7th, 2011)*.
30. R. A. Rakitov, Secretory products of the Malpighian tubules of Cicadellidae (Hemiptera, Membracoidea): an ultrastructural study. *International Journal of Insect Morphology and Embryology*. 28, 179–193 (1999).
31. J. Stam, "Diffraction shaders" in *Proceedings of the 26th annual conference on Computer graphics and interactive techniques - SIGGRAPH '99 (ACM Press, New York, New York, USA, 1999)*, pp. 101–110.
32. C. P. van den Berg, J. Troscianko, J. A. Endler, N. J. Marshall, K. L. Cheney, Quantitative Colour Pattern Analysis (QCPA): A comprehensive framework for the analysis of colour patterns in nature. *Methods in Ecology and Evolution*. 11, 316–332 (2020).
33. X. Zhou, P. Tian, C.-W. Sher, J. Wu, H. Liu, R. Liu, H.-C. Kuo, Growth, transfer printing and colour conversion techniques towards full-colour micro-LED display. *Progress in Quantum Electronics*. 71, 100263 (2020).

34. S. A. Morin, R. F. Shepherd, S. W. Kwok, A. A. Stokes, A. Nemiroski, G. M. Whitesides, Camouflage and Display for Soft Machines. *Science*. 337, 828–832 (2012).
35. Y. Fu, H. Zhao, Y. Wang, D. Chen, Z. Yu, J. Zheng, S. Sun, W. Cai, H. Zhou, Reversible Photochromic Photonic Crystal Device with Dual Structural Colors. *ACS Applied Materials & Interfaces*. 14, 29070–29076 (2022).
36. M. Abdolahi, H. Jiang, B. Kaminska, Structural colour QR codes for multichannel information storage with enhanced optical security and life expectancy. *Nanotechnology*. 30, 405301 (2019).
37. B. Ko, T. Badloe, Y. Yang, J. Park, J. Kim, H. Jeong, C. Jung, J. Rho, Tunable metasurfaces via the humidity responsive swelling of single-step imprinted polyvinyl alcohol nanostructures. *Nature Communications*. 13 (2022), doi:10.1038/s41467-022-32987-6.
38. A. E. Savakis, H. J. Trussell, On the accuracy of PSF representation in image restoration. *IEEE Transactions on Image Processing*. 2, 252–259 (1993).
39. Y.-Q. Liu, X. Du, H.-L. Shen, S.-J. Chen, Estimating Generalized Gaussian Blur Kernels for Out-of-Focus Image Deblurring. *IEEE Transactions on Circuits and Systems for Video Technology*. 31, 829–843 (2021).
40. E. D. Palik, *Handbook of optical constants of solids* (Academic Press, Orlando, 1985).

Acknowledgments

Funding: This work is funded by the Office of Navy Research (Awards #N0014-20-1-2095 and #N00014-21-1-2337). This work is also partially funded by the National Science Foundation (Grant No. CBET-1931964) and Defense Threat Reduction Agency (Grant No. HDTRA1-19-1-0028).

Author Contributions: The authors would also like to acknowledge the help from Dr. Lin Jing and Xiao Luo for the characterization of the samples. Z.L. and S.S. conceptualized, designed, and interpreted the experiments. L.W. and T.S.W. designed, modeled, and fabricated brochosome-like pixels. Z.L. and J. L. performed the FDTD simulations. X.L. and Z.L. conducted the experiments. Z.L. and S.S. wrote the manuscript with inputs from L.W., H.S.Y., Z.W., X.Z., and T.S.W.

Competing interests: T.S.W, L.W., S.S., and Z.L. are listed as inventors on an invention disclosure of U.S. patent application from the Pennsylvania State University and Carnegie Mellon University, which describe the design and working principle of the reported brochosome-like pixel twins for visible camouflage and infrared display.

Data and materials availability: All data supporting this work are available in the main text, extended data, and the Supplementary information, or from the corresponding author upon request.

Supplementary information

Supplementary Note

Figure S1 Design of brochosome-like pixels (BLPs).

Figure S2 Long-wavelength field profiles showing the cutoff effect of BLP absorption.

Figure S3 Necessity and effectiveness of brochosome-like pixels.

Figure S4 Scanning electron microscopy (SEM) images and element mapping results of a typical BLP array.

Figure S5 Quantitative analysis of visible images of BLP arrays.

Figure S6 Closely packed brochosome-like pixel array for high pixel-density display.

Figure S7 Tilted-angle thermal mapping measurements.

Figure S8 Quantitative analysis of camouflage and display under different imaging systems.

Figure S9 Optimization of infrared images of the BLP QR code.

Movie S1 Demonstration of real-time scanning of camouflaged QR code formed by brochosome-like pixels.

Supplementary Materials for
**Brochosome-inspired binary metastructures for pixel-by-pixel thermal
signature control**

Zhuo Li *et al.*

*Corresponding Email: sshen1@cmu.edu

This PDF file includes:

Supplementary Note

Figure S1 Design of brochosome-like pixels (BLPs).

Figure S2 Long-wavelength field profiles showing the cutoff effect of BLP absorption.

Figure S3 Necessity and effectiveness of brochosome-like pixels.

Figure S4 Scanning electron microscopy (SEM) images and element mapping results of a typical BLP array.

Figure S5 Quantitative analysis of visible images of BLP arrays.

Figure S6 Closely packed brochosome-like pixel array for high pixel-density display.

Figure S7 Tilted-angle thermal mapping measurements.

Figure S8 Quantitative analysis of camouflage and display under different imaging systems.

Figure S9 Optimization of infrared images of the BLP QR code.

Other Supplementary Materials for this manuscript include the following:

Movie S1 Demonstration of real-time scanning of camouflaged QR code formed by brochosome-like pixels.

Supplementary Note

Similarity between the BSDFs of the BLP twins

The similarity between the BSDFs of the BLP twins can be understood from the derivation provided by Jos Stam (see Ref. 31 in the main text) in which the refraction effect is considered. It has been shown that,

$$f_s(\mathbf{x}, \mathbf{k}_i, \mathbf{k}) \propto \langle |P(\mathbf{k}_x, \mathbf{k}_y)|^2 \rangle, \quad (\text{S1})$$

where

$$P(\mathbf{u}, \mathbf{v}) = \mathcal{F}[p(x, y)] = \mathcal{F}[e^{ik\omega h(x, y)}], \quad (\text{S2})$$

in which \mathcal{F} represents the Fourier transform and $z=h(x, y)$ is the height profile of considered scatter (in our case, the BLPs). Equations S1 and S2 show that the Fourier transform of the height profiles, and thus the spatial arrangement of the surface features determined the BSDFs of the BLPs, and consequently their visible region images. Therefore, by keeping the spatial arrangement of the pores the same while designing different the BLPs, one can ensure that they share similar appearances under the same illumination condition in a visible range imaging system, even though the detailed surface morphologies are different.

Supplementary figures

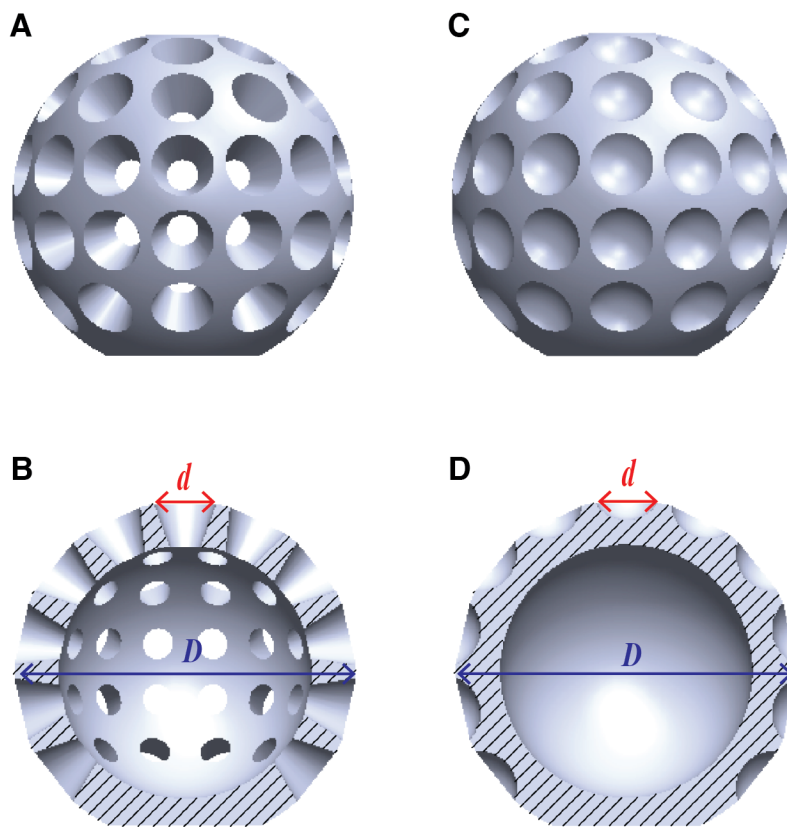


Fig. S1 | Design of brochosome-like pixels (BLPs). (A) – (B) Front view, and cross-sectional view of the op-BLPs. (C) – (D) Front view, and cross-sectional view of the cp-BLPs. d and D represent the diameters of the pores and the outer diameter of the BLPs, respectively.

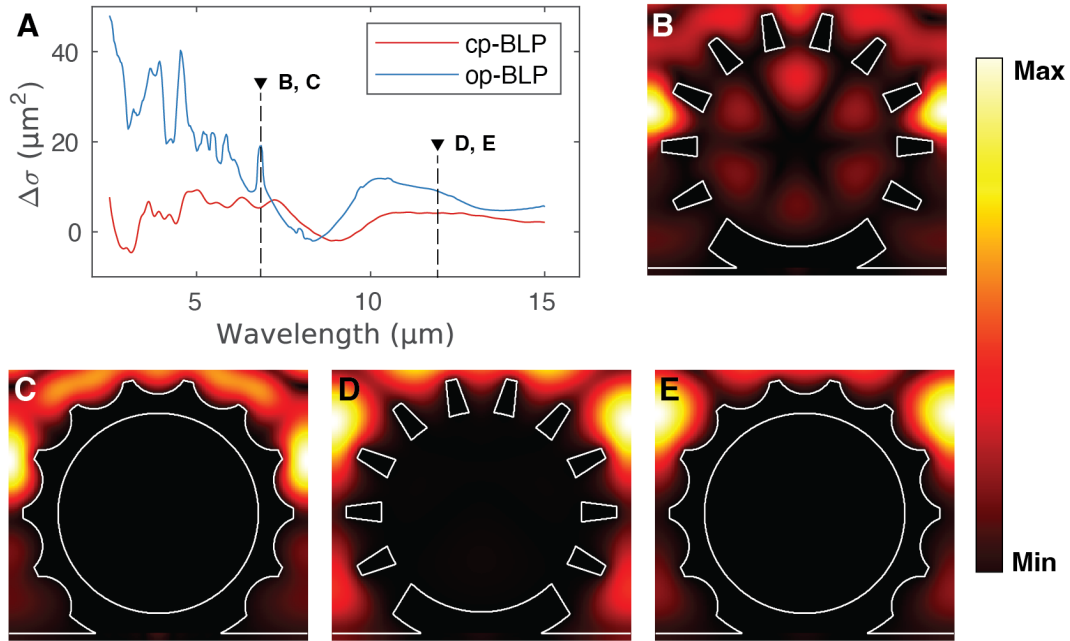


Fig. S2 | Long-wavelength field profiles showing the cutoff effect of the BLP absorption. (A) Simulated excess absorption cross sections with dashed lines marking the wavelengths at which the field profiles are plotted. **(B) – (C)** Field profiles near an op-BLP and a cp-BLP at the wavelength of 6.8 μm , respectively. **(D) – (E)**, Field profiles near an op-BLP and a cp-BLP at the wavelength of 11.9 μm , respectively.

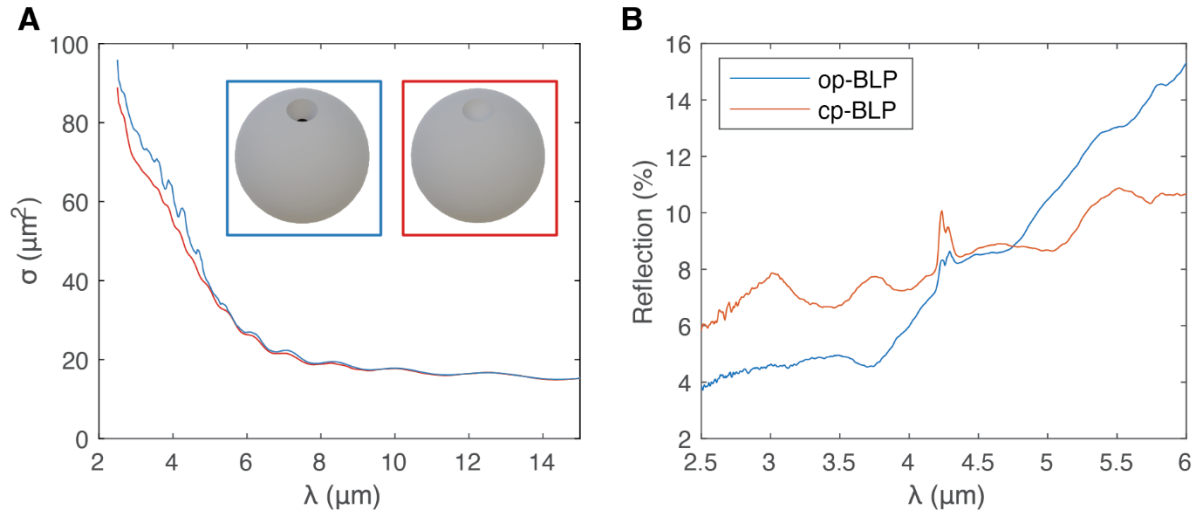


Fig. S3 | Necessity and effectiveness of brochosome-like pixels. (A) Simulated absorption cross sections of Hollow Ni spheres ($D = 20 \mu\text{m}$) with only one open/closed pore on the top, which show a much weaker contrast than those of op-BLP and cp-BLP. Inset: 3D models of the simulated structures. **(B)** Fourier-transform infrared reflection (FTIR) spectra of both the op-BLP and cp-BLP arrays showing the same infrared contrast of the two BLP structures.

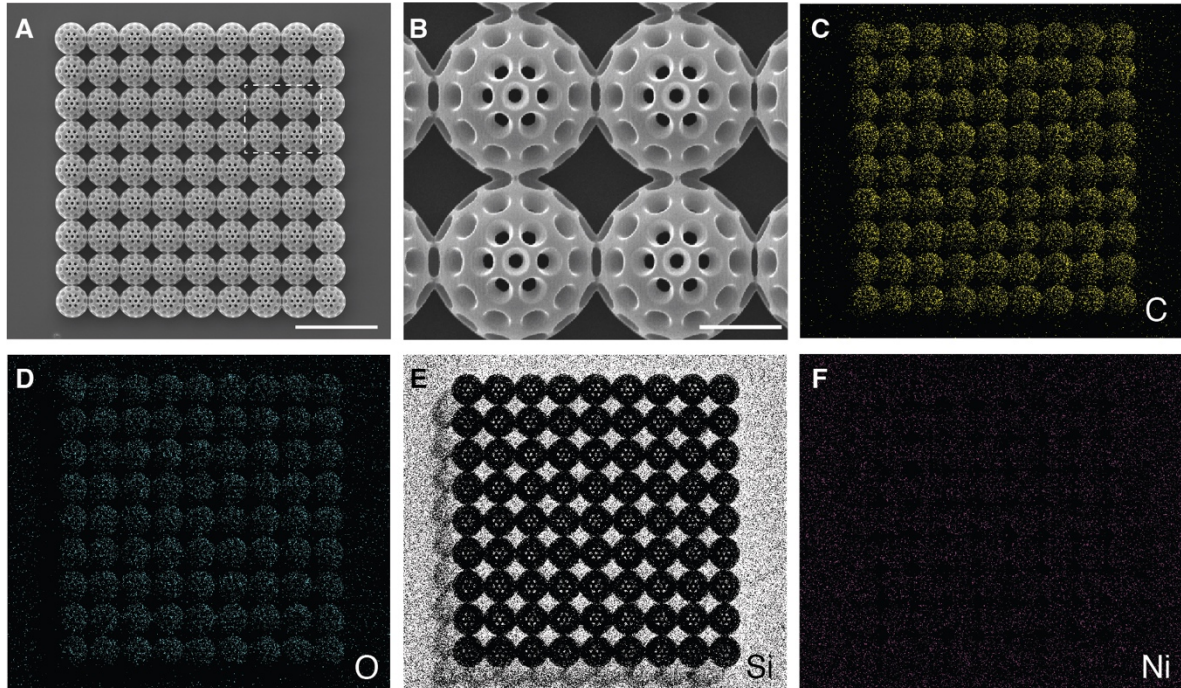


Fig. S4 | Scanning electron microscopy (SEM) images and element mapping results of a typical BLP array. (A) A SEM image of a Ni-coated 9-by-9 op-BLP array, scale bar 50 μm . **(B)** A zoom-in SEM image of the region marked by the white dashed box in **a**, scale bar: 10 μm . **(C) to (F)**, Element mapping results of the array shown in **(A)**. The scaffolds of the BLPs are printed with IP-DIP on a Si substrate, and then coated with ~ 100 nm thick Ni.

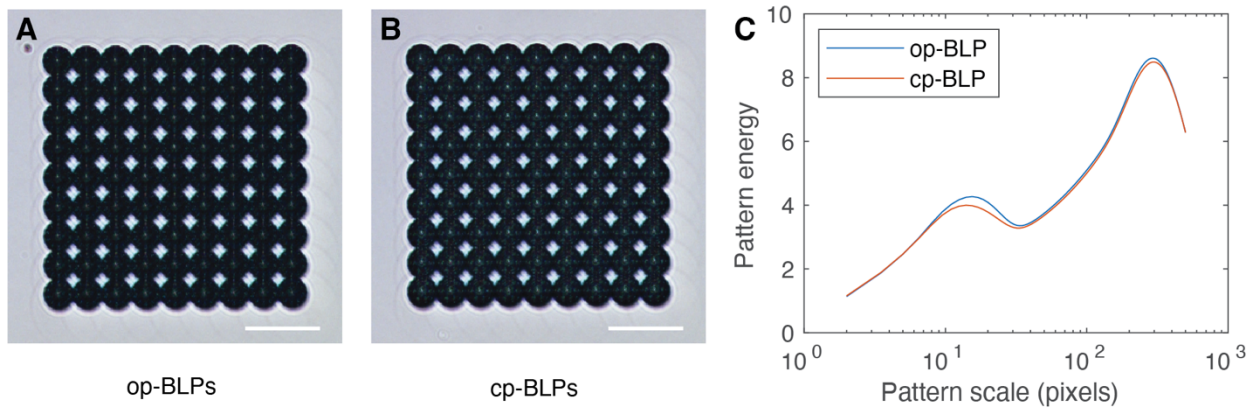


Fig. S5 | Quantitative analysis of visible images of the BLP arrays. (A) – (B) Images of a 9-by-9 op-BLP array and a 9-by-9 cp-BLP array, respectively. Images are imported to and processed by ImageJ for analysis. Scale bars: 50 μm . **(C)** Calculated pattern energy distribution among patterns of different sizes (measured by pixels in both the images) by the quantitative color pattern analysis method (see Ref. 32 in the main text). The two overlapped curves suggest that the two arrays appear almost identical in the visible range images.

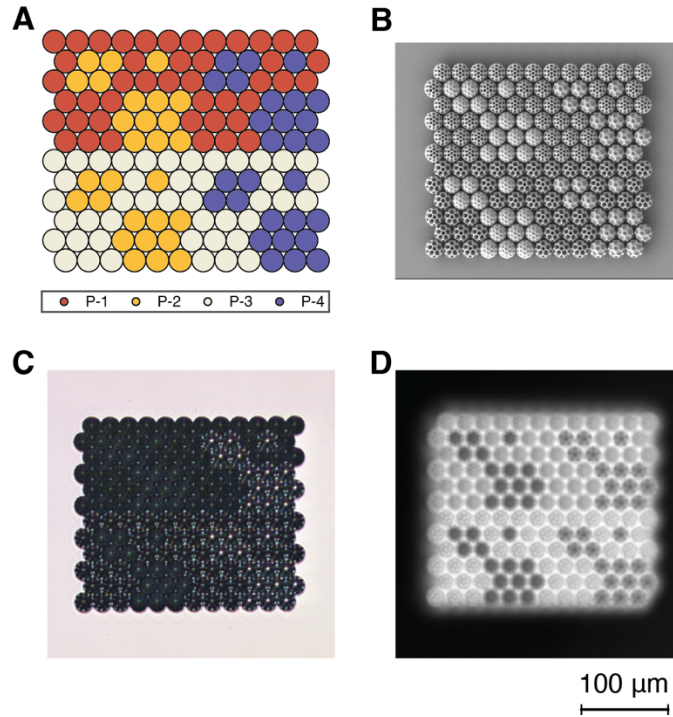


Fig. S6 | Closely packed brochosome-like pixel array for high pixel-density display. (A) BLPs with surface features of different shapes forming a closed packed array. P-1 to P-4 represent BLPs with round open pores ($d = 3.7 \mu\text{m}$), with round closed pores ($d = 3.7 \mu\text{m}$), with polygon open pores ($d = 4.5 \mu\text{m}$), and with polygon closed pores ($d = 4.5 \mu\text{m}$), respectively. **(B)** a SEM image of the closely packed BLP array. **(C) – (D)** An optical and an infrared images of the closely packed BLP array taken at $20\times$ magnification. The optimized BLP pairs also (P-1 and P-2) retain the visible range concealment and infrared contrast when they are closely packed.

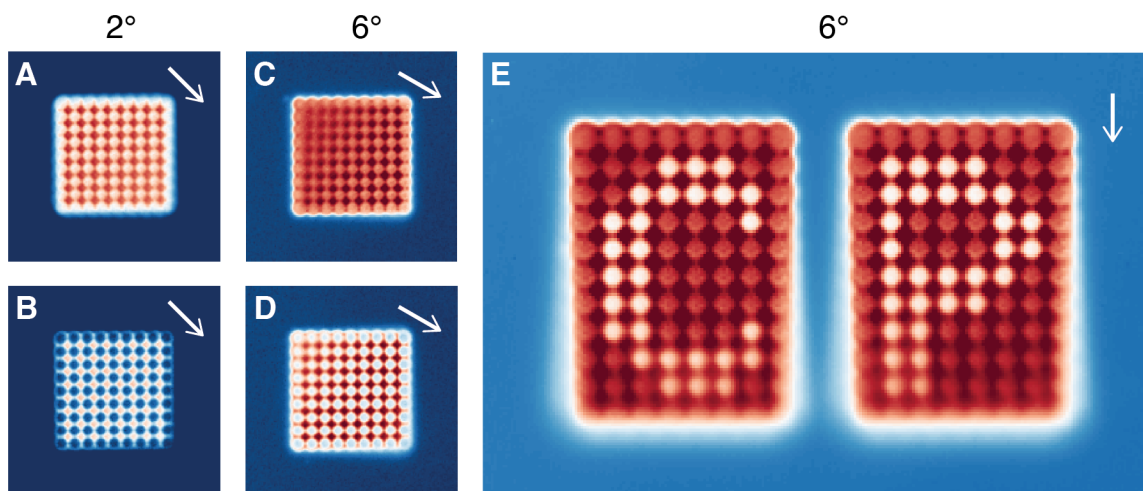


Fig. S7 | Tilted-angle thermal mapping measurements. (A) – (B) Infrared emissivity of an op-BLP array and a cp-BLP array respectively when tilted by 2 degrees. (C) – (D) Infrared emissivity of an op-BLP array and a cp-BLP array respectively when tilted by 6 degrees. (E) The arrays showing letters ‘C’ and ‘P’ when viewed with a 6-degree tilting. The bottom blurred part is out of focus, so extraction of patterned data at a larger tilting angle will be limited by the focal depth of microscopes. The tilted angles are estimated by comparing the sizes of the measured arrays to their original sizes. Arrows mark the ‘downhill’ direction of the tilted samples. IR images are captured with a 12× objective.

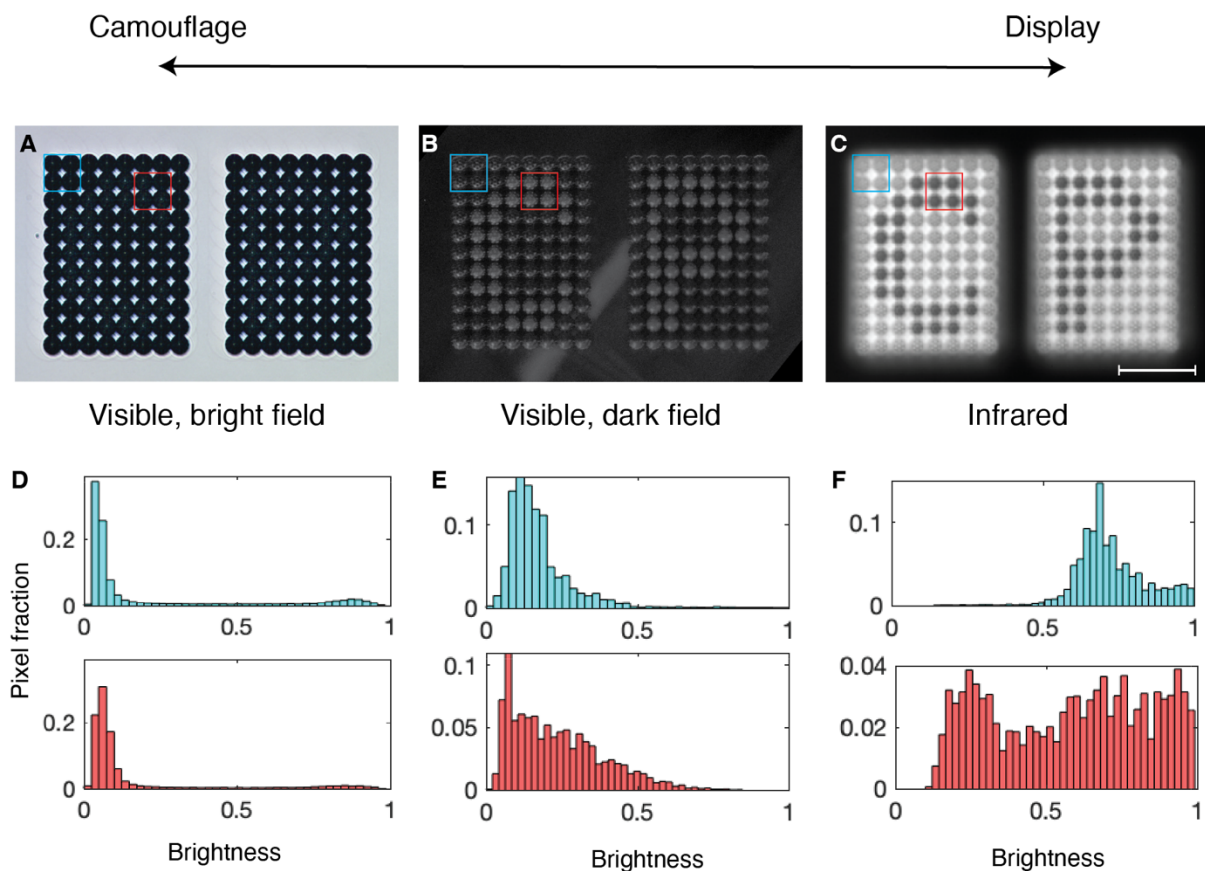


Fig. S8 | Quantitative analysis of camouflage and display under different imaging systems. (A) – (C) Images of BLP arrays taken under visible microscope in the bright field mode, dark field mode, and infrared microscope, respectively. Scale bar: 100 μm . (D) – (F) Pixels brightness distributions in the background (cyan) and patterns (red) for the three images, respectively. The analyzed regions are highlighted in the corresponding images by the cyan and red boxes, respectively. In the bright field image, pixel distributions in the background and pattern are nearly identical, providing maximum camouflage effect. In the dark field image, pixel distributions in the background and pattern follow similar trends but with a minor difference, which leads to a suppressed visibility of the ‘C’ and ‘P’ pattern. In the IR image, pixel brightness distributions in the background and pattern are significantly different, especially for brightness smaller than 0.5, which provides the optimized display effect. The analysis method is adopted from Ref. 34 in main text. Analyzed images are imported to MATLAB and converted to grayscale; pixel values are normalized to 0 to 1 before counting. Note here, ‘pixel’ refers to the real pixel forming the images, not the brochosome-like pixels we designed.

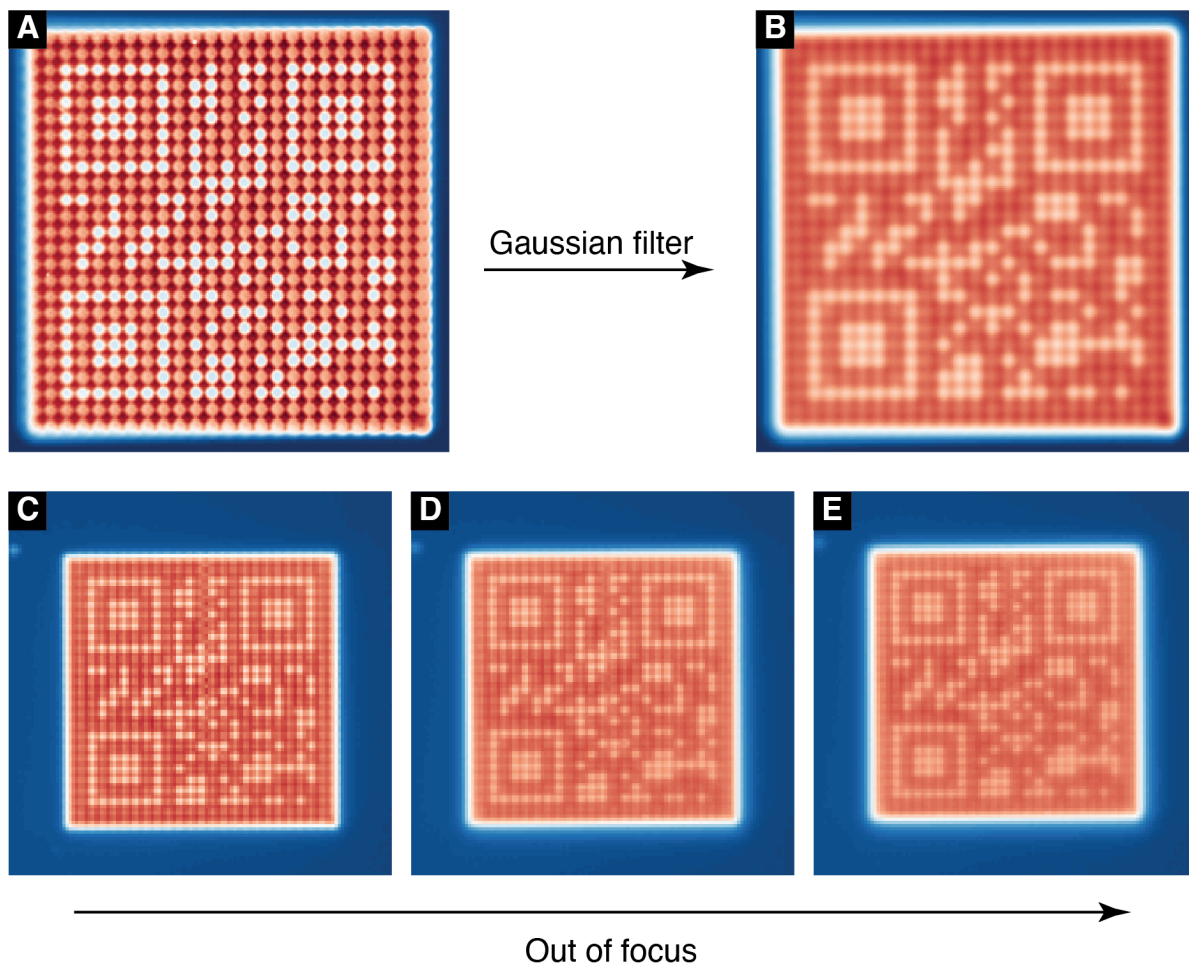


Fig. S9 | Optimization of infrared images of the BLP QR code. (A) – (B) Blurring the IR images by applying Gaussian filleters. The original IR image (A) is taken with a $12\times$ objective. 2-D Gaussian filter is applied to the original image in MATLAB to generate the blurred image (B). (C) – (E), Blurring the IR images by de-focusing the imaging system. Images are taken with a $4\times$ objective. IR images of the BLP QR code are easier to scan after proper blurring.